

Control of quantum coherence of photons exploiting quantum entanglement

Dianzhen Cui¹, Xi-Lin Wang,² X.X. Yi,¹ and Li-Ping Yang^{1,*}

¹*Center for Quantum Sciences and School of Physics, Northeast Normal University, Changchun 130024, China*

²*National Laboratory of Solid State Microstructures, School of Physics, Nanjing University, Nanjing 210093, China*



(Received 16 September 2023; revised 2 January 2024; accepted 25 January 2024; published 9 February 2024)

Accurately controlling the quantum coherence of photons is pivotal for their applications in quantum sensing and quantum imaging. Here, we propose the utilization of quantum entanglement and local phase manipulation techniques to control the higher-order quantum coherence of photons. By engineering the spatially varying phases in the transverse plane, we can precisely manipulate the spatial structure of the second-order coherence function of entangled photon pairs without changing the photon intensity distribution of each photon. Our approach can readily be extended to higher-order quantum coherence control. These results could potentially stimulate experimental research and applications of optical quantum coherence.

DOI: 10.1103/PhysRevApplied.21.024019

I. INTRODUCTION

Three are three main quantum resources of photons having been utilized for quantum-enhanced technologies [1–3]: quantum states of photons with reduced quantum fluctuations, such as squeezed coherent states [4–6]; quantum entanglement, which characterizes the global quantum correlations between photons, such as NOON states [7,8] and polarization entanglement [9,10]; and higher-order quantum coherence arising from the statistical correlation of electromagnetic fields at multiple space-time points [11]. Spatial correlation and quantum entanglement of photons have been widely used to enhance the signal-to-noise ratio in quantum imaging [12–15] and increase the sensitivity in phase measurements with weak quantum light [16–18]. Spatial-polarization hyperentangled photon pairs have been used for quantum holography of complex objects [19] and quantum-enhanced phase imaging [20,21]. Remarkable progress has been made in leveraging both two-body quantum entanglement and the spatial quantum coherence of photon pairs for a variety of valuable applications [22–24]. Here, we present a theoretical framework aimed at actively manipulating the spatial structure of higher-order quantum coherence of photons through the utilization of quantum entanglement.

The spatial coherence of a photon pair generated through the spontaneous parametric down-conversion (SPDC) process is primarily determined by the characteristics of the pump laser and the nonlinear media [25,26]. The recent

advancements in precisely manipulating the transverse spatial properties of photons [27–30] have provided us with powerful tools to further control the quantum coherence of photon pairs after they exit the source. Transfer of entanglement between the spin and orbital angular momentum (OAM) degrees of photons has been achieved using techniques such as a q -plate, a spatial light modulator (SLM), a structured metasurface [31,32], or structured geometric phase grating [33]. However, previous research has mainly focused on the global entanglement between the two photons. The precise manipulation of the detailed spatial structure of second-order quantum coherence in two-photon states is particularly intriguing, as it has the potential to unlock valuable quantum resources within structured photon pairs for quantum imaging [12,34–36] and quantum sensing [37–40].

In previous work [41], the coherence function of an entangled vortex pair has been shown to be modulated by the helical phases of the photons. Recently, this effect has been experimentally demonstrated [24,42,43]. In this paper, we propose a general theoretical frame for the precise manipulation of higher-order quantum coherence of photons. By engineering the phases of the photons in their transverse plane, we can tailor the spatial structure of the quantum coherence function of photon pairs on demand, while keeping the photon-number density distribution unchanged. This method can be applied for higher-order quantum optical coherence control. Due to the progress in precise manipulation of single-photon wave fronts [44,45], our method could inspire captivating experiments and applications that harness the quantum coherence of photons.

*lipingyang87@gmail.com

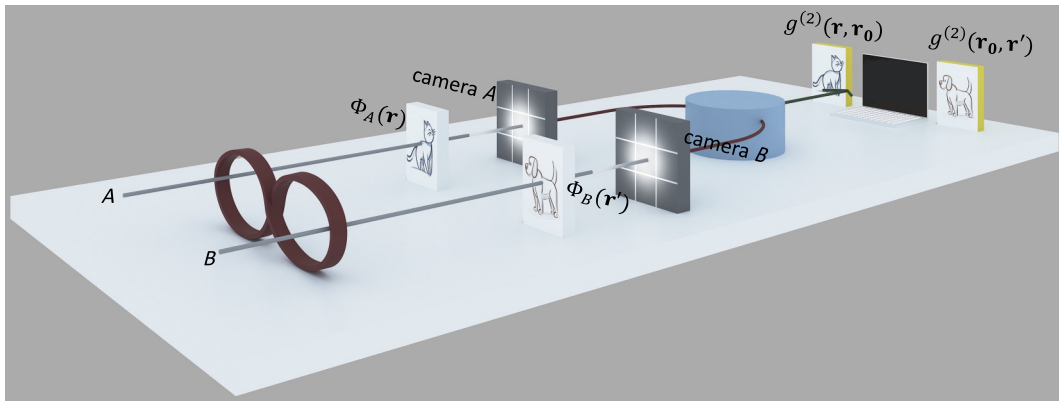


FIG. 1. Manipulation of quantum coherence of entangled photon pairs. SLMs are utilized to impose transverse-plane phases $\Phi_A(\mathbf{r})$ and $\Phi_B(\mathbf{r}')$ on the two photons, respectively. These two phases modify the second-order coherence function $g^{(2)}(\mathbf{r}, \mathbf{r}')$ of photon pairs while leaving their photon-number density distributions unchanged.

The paper is organized as follows. In Sec. II, we present the method to control the spatial structure of the second-order quantum coherence of entangled photon pairs. In Sec. III, we demonstrate the coherence control of product-state photon pairs via Hong-Ou-Mandel (HOM) interference. Manipulation of higher-order coherence of photons is elucidated in Sec. IV. The conclusions are summarized in Sec. V.

II. CONTROL QUANTUM COHERENCE VIA SPATIALLY VARYING PHASES

Paraxial photon pairs generated through SPDC have been routinely used in quantum sensing and quantum imaging [15,46–48]. Two paraxial photons propagating in different directions are spatially distinguishable. For convenience, we can employ two coordinate frames with path labels A and B [see more details in the Appendix] to expand the WPF of each pulse in its respective frame [49–51]

$$\begin{aligned} |P_\xi\rangle &= \sum_{\lambda\lambda'} \int d\mathbf{k}_A \int d\mathbf{k}'_B \tilde{\xi}_{\lambda\lambda'}(\mathbf{k}_A, \mathbf{k}'_B) \hat{a}_{\mathbf{k}_A, \lambda}^\dagger(t) \hat{b}_{\mathbf{k}'_B, \lambda'}^\dagger(t) |0\rangle, \\ &= \sum_{\lambda\lambda'} \int d\mathbf{r}_A \int d\mathbf{r}'_B \tilde{\xi}_{\lambda\lambda'}(\mathbf{r}_A, \mathbf{r}'_B, t) \hat{\psi}_{a, \lambda}^\dagger(\mathbf{r}_A) \hat{\psi}_{b, \lambda'}^\dagger(\mathbf{r}'_B) |0\rangle, \end{aligned} \quad (1)$$

where the wave-packet function (WPS) $\xi_{\lambda\lambda'}(\mathbf{r}_A, \mathbf{r}'_B, t)$ is the Fourier transformation of the spectrum amplitude function (SAF) $\tilde{\xi}_{\lambda\lambda'}(\mathbf{k}_A, \mathbf{k}'_B)$ in wave-vector space [52], \mathbf{r}_A (\mathbf{k}_A) and \mathbf{r}'_B (\mathbf{k}'_B) are the coordinates (wave vectors) of the two-photon pulses, and λ is the polarization index. Usually, cylindrical coordinates $\mathbf{r} = \rho + z\mathbf{e}_z = \rho \cos \varphi \mathbf{e}_x + \rho \sin \varphi \mathbf{e}_y + z\mathbf{e}_z$ (\mathbf{e}_i is the unit vector of i axis) and $\mathbf{k} = \tilde{\rho} + k_z \mathbf{e}_z = \tilde{\rho} \cos \tilde{\varphi} \mathbf{e}_x + \tilde{\rho} \sin \tilde{\varphi} \mathbf{e}_y + k_z \mathbf{e}_z$ are employed to expand the WPF and SAF of paraxial photons. The two paraxial pulses can be approximately treated as two spatially independent modes. Consequently, the ladder (field)

operators of two photons commute with each other [52], i.e., $[\hat{a}_{\mathbf{k}_A, \lambda}, \hat{b}_{\mathbf{k}'_B, \lambda'}^\dagger] = 0$ and $[\hat{\psi}_{a, \lambda}(\mathbf{r}_A), \hat{\psi}_{b, \lambda'}^\dagger(\mathbf{r}'_B)] = 0$. In the following, we will omit the path labels A and B in the coordinates and wave vectors for conciseness.

Usually, the time-varying $g^{(2)}(\tau)$ function is used to characterize the bunching and antibunching property of a quasi-one-dimensional photon pulses propagating in z direction. To characterize the spatial correlations of structured photon pairs, we focus on the second-order coherence function for paraxial light pulses [11,41]

$$g_{\lambda\lambda'}^{(2)}(\mathbf{r}, \mathbf{r}') = \frac{G_{\lambda\lambda'}^{(2)}(\mathbf{r}, \mathbf{r}')}{\langle \hat{n}_{a, \lambda}(\mathbf{r}) \rangle \langle \hat{n}_{b, \lambda'}(\mathbf{r}') \rangle}, \quad (2)$$

where $G_{\lambda\lambda'}^{(2)}(\mathbf{r}, \mathbf{r}') = \langle \hat{\psi}_{a, \lambda}^\dagger(\mathbf{r}) \hat{\psi}_{b, \lambda'}^\dagger(\mathbf{r}') \hat{\psi}_{b, \lambda'}(\mathbf{r}') \hat{\psi}_{a, \lambda}(\mathbf{r}) \rangle$ is the equal-time two-point intensity correlation function and the photon-number densities $\langle \hat{n}_{a, \lambda}(\mathbf{r}) \rangle = \langle \hat{\psi}_{a, \lambda}^\dagger(\mathbf{r}) \hat{\psi}_{a, \lambda}(\mathbf{r}) \rangle$ and $\langle \hat{n}_{b, \lambda'}(\mathbf{r}') \rangle = \langle \hat{\psi}_{b, \lambda'}^\dagger(\mathbf{r}') \hat{\psi}_{b, \lambda'}(\mathbf{r}') \rangle$ of the two photons. Prior research has shown that the $g^{(2)}$ function of entangled vortex photon pairs undergoes modulation due to their helical phases [53]. Here, we present a comprehensive approach for manipulating the spatial structure of photonic quantum coherence as shown in Fig. 1.

A. Momentum-correlation-removed photon pairs

Usually, two photons generated from SPDC are correlated in both frequency and momentum due to the energy conservation and phase-matching conditions. Using a narrow-bandwidth filter or a single-mode fiber, these correlations can be removed without compromising their polarization entanglement. We start with a polarization-entangled photon pair with WPF $\xi_{\lambda\lambda'}(\mathbf{r}, \mathbf{r}') = \eta_A(\mathbf{r})\eta_B(\mathbf{r}')\Theta_{\lambda\lambda'}$, where $\eta_A(\mathbf{r})$ [$\eta_B(\mathbf{r}')$] describes the shape of the photon A (B) and the 2×2 matrix $\Theta_{\lambda\lambda'}$ characterize the polarization state. Without loss of generality, we

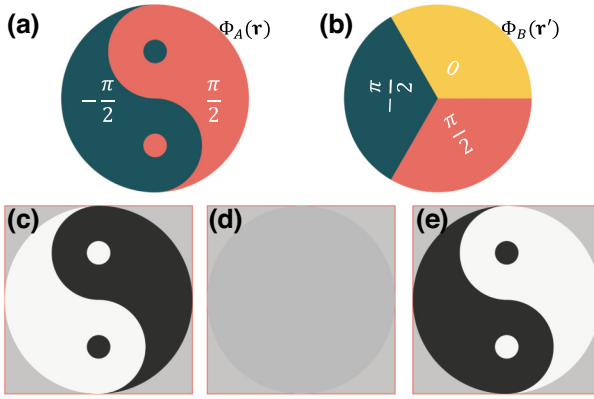


FIG. 2. (a),(b) Phase patterns applied on photon A and photon B , respectively. (c)–(e) Coincidence images obtained from photon A when \mathbf{r}' of photon B is anchored in the regions with $\Phi_B(\mathbf{r}') = \pi/2$, $\Phi_B(\mathbf{r}') = 0$, and $\Phi_B(\mathbf{r}') = -\pi/2$, respectively.

consider the polarization-entangled state

$$\Theta_{\lambda\lambda'} = \frac{1}{\sqrt{2}}(\delta_{\lambda,H}\delta_{\lambda',V} + \delta_{\lambda,V}\delta_{\lambda',H}). \quad (3)$$

Our method can be directly applied to other entangled photon pairs. To modulate the quantum coherence function, two polarization-sensitive SLMs are utilized to impose distinct phase patterns onto the two photons

$$\xi_{\lambda\lambda'}(\mathbf{r}, \mathbf{r}') = \frac{\eta_A(\mathbf{r})\eta_B(\mathbf{r}')}{\sqrt{2}} \times \left[\delta_{\lambda,H}\delta_{\lambda',V}e^{i\Phi_A(\mathbf{r})} + \delta_{\lambda,V}\delta_{\lambda',H}e^{i\Phi_B(\mathbf{r}')} \right]. \quad (4)$$

Here, spatially varying phases $\Phi_A(\mathbf{r})$ and $\Phi_B(\mathbf{r}')$ have only been added to the $|H\rangle$ -state photons. Usually, a SLM only changes the phase of photons within their transverse plane. However, our approach can apply to cases involving three-dimensional structured phases as well.

The added phases do not change the field-intensity distributions of the two photons, i.e., $\langle \hat{n}_{a,\lambda}(\mathbf{r}) \rangle = |\eta_A(\mathbf{r})|^2/2$ and $\langle \hat{n}_{b,\lambda}(\mathbf{r}') \rangle = |\eta_B(\mathbf{r}')|^2/2$. Furthermore, we can confirm that the applied phase cannot be extracted using polarization filters, such as circular-polarization projections

$$\langle \hat{\psi}_{a,L}^\dagger(\mathbf{r})\hat{\psi}_{a,L}(\mathbf{r}) \rangle = \langle \hat{\psi}_{a,R}^\dagger(\mathbf{r})\hat{\psi}_{a,R}(\mathbf{r}) \rangle = \frac{1}{2}|\eta_A(\mathbf{r})|^2, \quad (5)$$

$$\langle \hat{\psi}_{b,L}^\dagger(\mathbf{r}')\hat{\psi}_{b,L}(\mathbf{r}') \rangle = \langle \hat{\psi}_{b,R}^\dagger(\mathbf{r}')\hat{\psi}_{b,R}(\mathbf{r}') \rangle = \frac{1}{2}|\eta_B(\mathbf{r}')|^2, \quad (6)$$

with field operators $\hat{\psi}_L(\mathbf{r}) = [\hat{\psi}_H(\mathbf{r}) + i\hat{\psi}_V(\mathbf{r})]/\sqrt{2}$ and $\hat{\psi}_R(\mathbf{r}) = [\hat{\psi}_H(\mathbf{r}) - i\hat{\psi}_V(\mathbf{r})]/\sqrt{2}$. Finally, we measure the

second-order coherence function associated with the correlation between two left-circular-polarization states

$$g_{LL}^{(2)}(\mathbf{r}, \mathbf{r}') = 1 + \cos[\Phi_A(\mathbf{r}) + \Phi_B(\mathbf{r}')]. \quad (7)$$

By manipulating the phases $\Phi_A(\mathbf{r})$ and $\Phi_B(\mathbf{r}')$, we can tailor the spatial structure of the quantum coherence of a photon pair for purpose, such as incorporating a cat onto photon A and a dog onto photon B (see Fig. 1). A similar coherence function can be obtained for right-circularly polarized photons.

To extract the image encoded in the phases, we can anchor one of the coordinates (e.g., by setting $\mathbf{r}' = \mathbf{r}_0$) within the coherence function $g_{LL}^{(2)}(\mathbf{r}, \mathbf{r}_0)$ and scan the other coordinate. As illustrated in Fig. 2, we imprint a Taiji pattern [panel (a)] on photon A and a three-sector pattern [panel (b)] on photon B . For the fixing \mathbf{r}' in the region where $\Phi_B(\mathbf{r}') = \pi/2$, the pattern in panel (c) will be observed in coincidence imaging. Similarly, fixing \mathbf{r}' in the regions where $\Phi_B(\mathbf{r}') = 0$ and $\Phi_B(\mathbf{r}') = -\pi/2$, the patterns depicted in panels (d) and (e), respectively, will be obtained from the measured coherence functions.

B. Strongly correlated photon pairs

The coherence function of photon pairs with momentum correlations is typically modified by added phases as well as the intensity distributions, unlike the simple result in Eq. (7). A uniformly polarized photon pair generated through SPDC processes can be generally described by a SAF [54–56] $\tilde{\xi}_{\lambda\lambda'}(\mathbf{k}, \mathbf{k}') = \tilde{\eta}(k_z, k'_z)\tilde{\mathcal{E}}(\tilde{\rho} + \tilde{\rho}')\tilde{\chi}(\tilde{\rho} - \tilde{\rho}')\Theta_{\lambda,\lambda'}$. Here, the function $\tilde{\eta}(k_z, k'_z)$ determines the shapes of the two photons along their propagating directions, while $\tilde{\mathcal{E}}(\tilde{\rho} + \tilde{\rho}')$ characterizes the angular profile of the pump beam in the transverse plane. The phase-matching condition can be described by

$$\tilde{\chi}(\tilde{\rho} - \tilde{\rho}') = \frac{1}{\pi}\sqrt{\frac{2L}{k_0}}\text{sinc}\left(\frac{L|\tilde{\rho} - \tilde{\rho}'|^2}{4k_0}\right), \quad (8)$$

where k_0 is the wave number of the pump and L is the thickness of the nonlinear crystal. For a pump with a flat transverse distribution, the function $\tilde{\mathcal{E}}(\tilde{\rho} + \tilde{\rho}')$ approaches a Dirac δ function $\delta(\tilde{\rho} + \tilde{\rho}')$. While for a thin crystal, the sinc function is relatively flat in the momentum space and its Fourier transformation could be approximated as a δ function $\chi(\rho - \rho') \approx \delta(\rho - \rho')$ [20,21]. In this case, two photons are strongly correlated in momentum, as well as in real space.

We illuminate a particular case, in which a structured phase $\Phi_B(\rho')$ is only applied to photon B as shown in Fig. 3(a). The WPF function of the photon pair after the SLM can be obtained through Fourier transformation of

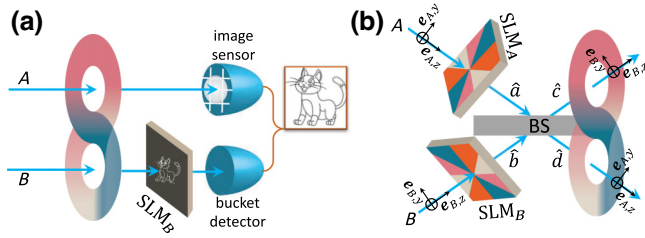


FIG. 3. (a) Controlling the quantum coherence of strongly correlated pairs. The pattern applied on the phase of photon B can be extracted from coincidence imaging from an imaging sensor in path A . (b) Controlling the quantum coherence of product-state photon pairs with HOM interference.

the SAF

$$\xi_{\lambda\lambda'}(\mathbf{r}, \mathbf{r}') = \frac{1}{\sqrt{2}} \eta(z, z') \mathcal{E}(\rho + \rho') \chi(\rho - \rho') \times [\delta_{\lambda, H} \delta_{\lambda', V} + \delta_{\lambda, V} \delta_{\lambda', H} e^{i\Phi_B(\rho')}] . \quad (9)$$

In the absence of momentum correlations, the structured phase on photon B can solely be extracted by the image sensor in path B . However, for a strongly correlated photon pair with $\chi(\rho - \rho') \approx \delta(\rho - \rho')$, the phase Φ_B can also be extracted by a camera in path A via coincidence measurements

$$g_{\text{eff}}^{(2)}(\rho) = \frac{\int d\mathbf{r}' \langle \hat{\psi}_{a,L}^\dagger(\mathbf{r}) \langle \hat{\psi}_{b,L}^\dagger(\mathbf{r}') \hat{\psi}_{b,L}(\mathbf{r}') \rangle \hat{\psi}_{a,L}(\mathbf{r}) \rangle}{\langle \hat{\psi}_{a,L}^\dagger(\mathbf{r}) \hat{\psi}_{a,L}(\mathbf{r}) \rangle} \quad (10)$$

$$= \frac{1}{2} [1 + \cos \Phi_B(\rho)] . \quad (11)$$

This is similar to the ghost imaging [57], but here we focus more on using quantum entanglement to control the quantum coherence of photon pairs.

C. Influence of diffraction

In previous sections, the influence of light diffraction during propagation has not been taken into account. When dealing with a quasi-single-frequency pulse, the pulse's propagation can be effectively handled using the angular spectrum method [58]. Usually, the envelopes of paraxial photon pulses in the propagating directions are relatively flat in experiments. The image signal captured by an image sensor is characterized by the integral intensity over a finite distance ($\delta z = c\delta t$), where δt represents the exposure time and δz significantly exceeds the pulse length. In such instances, we need only to consider the propagation of a

single plane, such as the center plane $z = z_C$ of each pulse,

$$\begin{aligned} & \xi_{\lambda\lambda'}(\rho, z_C; \rho', z'_C) \\ &= \frac{1}{\sqrt{2}} \eta_A(\rho, z_C) \eta_B(\rho', z'_C) \left[\delta_{\lambda, H} \delta_{\lambda', V} e^{i\Phi_A(\rho)} \right. \\ &\quad \left. + \delta_{\lambda, V} \delta_{\lambda', H} e^{i\Phi_B(\rho')} \right] . \end{aligned} \quad (12)$$

Without loss of generality, we designate the SLM plane as the $z = 0$ plane and set $z_C = 0$ at $t = 0$. After a propagating distance $z = ct$ (t is the traveling time), the two-photon wave packet undergoes a transformation [58]

$$\xi_{\lambda\lambda'}(\rho, z; \rho', z') = \xi_{\lambda\lambda'}(\rho, 0; \rho', 0) \circledast H(\rho, z) \circledast H(\rho', z'), \quad (13)$$

where \circledast denotes the convolution and the propagator in space is given by

$$H(x, y, z) = \int dk_x \int dk_y e^{i(k_x x + k_y y + k_z z)} . \quad (14)$$

For paraxial pulses, we can linearize the square root function to the first order, yielding $k_z \approx k_i - (k_x^2 + k_y^2)/2k_i$, where k_i is the center wave number of the pulse in path i . In this case, the amplitude function $\eta_i(\rho)$ will mix with the phase function $\Phi_i(\rho)$ during the convolution process. Consequently, the pattern extracted from the $g^{(2)}(\rho, \rho')$ image tends to blur significantly over large propagating distances.

In experiments [19,43], $4f$ systems have been used to address this issue, as illustrated in Fig. 4. We now consider the case where the SLM is positioned at the front focal plane of the first lens, and the detector is situated at the rear focal plane of the second lens. The expression for the two-photon wave packet at the detector, considering two lenses with identical focal lengths f , is given by [59]

$$\begin{aligned} & \xi_{\lambda\lambda'}(\rho, \rho') \\ &= \frac{k_A^2 k_B^2}{f^4} e^{i8\pi(k_A+k_B)f} \int d\rho_1 \int d\rho_2 \mathcal{P}\left(\frac{k_A}{f}\rho + \frac{k_A}{f}\rho_1\right) \\ &\quad \times \mathcal{P}\left(\frac{k_B}{f}\rho' + \frac{k_B}{f}\rho_2\right) \xi_{\lambda\lambda'}(\rho_1, 0; \rho_2, 0), \end{aligned} \quad (15)$$

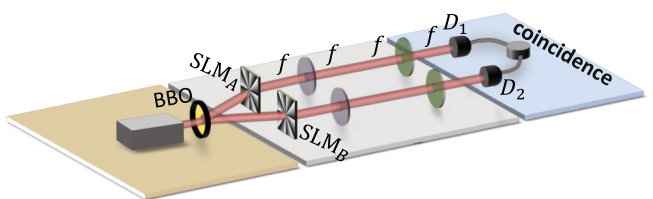


FIG. 4. The $4f$ systems are utilized to alleviate the blur effect resulting from diffraction. In each path, the SLM is positioned at the front focal plane of the first lens, while the detector is situated at the rear focal plane of the second lens.

where $\mathcal{P}(\tilde{\rho})$, which is the Fourier transform of the pupil function, reduces to a δ function $\delta(\tilde{\rho})$ for ideal lenses. The observed coherence function will be characterized by Eq. (7).

III. COHERENCE CONTROL VIA HOM INTERFERENCE

Our method primarily relies on the utilization of global entanglement to manipulate the detailed spatial structure of the quantum coherence functions. HOM interference is a viable approach for generating two-path entanglement [22], enabling effective manipulation of the optical coherence even for product-state photon pairs as depicted in Fig. 3(b). When two linearly polarized photons are initially in a product state, the WPF of the resulting photon pair after the SLMs can be expressed as follows:

$$\xi(\mathbf{r}, \mathbf{r}') = \eta_A(\mathbf{r})\eta_B(\mathbf{r}')e^{i[\Phi_A(\mathbf{r})+\Phi_B(\mathbf{r}')]}, \quad (16)$$

where the real functions $\Phi_A(\mathbf{r})$ and $\Phi_B(\mathbf{r}')$ denote the phases imposed on the two photons, respectively. For simplicity, we assume that $\eta_A(\mathbf{r})$ and $\eta_B(\mathbf{r}')$ possess axial symmetry and are independent of the azimuthal angles φ and φ' . However, we note that our approach

can be extended to encompass more general scenarios as well.

The complete theory of HOM interference for structured photon pairs encompassing spectral, polarization, and spatial degrees of freedom has been established [50] (see more details in the Appendix) and further extended to mixed-state photon pairs [51]. Here, we show that the phases added by SLMs do not affect the photon-number density distribution of photon pulse at each output channel of an HOM interferometer

$$\langle \Psi_{\text{out}} | \hat{\psi}_c^\dagger(\mathbf{r})\hat{\psi}_c(\mathbf{r}) | \Psi_{\text{out}} \rangle = \frac{1}{2} [|\eta_A(\mathbf{r})|^2 + |\eta_B(\mathbf{r})|^2], \quad (17)$$

$$\langle \Psi_{\text{out}} | \hat{\psi}_d^\dagger(\mathbf{r})\hat{\psi}_d(\mathbf{r}) | \Psi_{\text{out}} \rangle = \frac{1}{2} [|\eta_A(\mathbf{r})|^2 + |\eta_B(\mathbf{r})|^2], \quad (18)$$

where $|\Psi_{\text{out}}\rangle$ is the output state after HOM interference (see more details in the Appendix). The terms involving the phases Φ_A and Φ_B undergo complete cancellation due to the destructive interference occurring between the output bunching and antibunching photons [52]. However, the added two phases change the two-port $g^{(2)}$ function of output photons significantly

$$g_{cd}^{(2)}(\mathbf{r}, \mathbf{r}') = \frac{\langle \Psi_{\text{out}} | \hat{\psi}_d^\dagger(\mathbf{r})\hat{\psi}_c^\dagger(\mathbf{r}')\hat{\psi}_c(\mathbf{r}')\hat{\psi}_d(\mathbf{r}) | \Psi_{\text{out}} \rangle}{\langle \Psi_{\text{out}} | \hat{\psi}_d^\dagger(\mathbf{r})\hat{\psi}_d(\mathbf{r}) | \Psi_{\text{out}} \rangle \langle \Psi_{\text{out}} | \hat{\psi}_c^\dagger(\mathbf{r}')\hat{\psi}_c(\mathbf{r}') | \Psi_{\text{out}} \rangle} \quad (19)$$

$$= \frac{|\eta_A(\mathbf{r})|^2|\eta_B(\mathbf{r}')|^2 + |\eta_B(\mathbf{r})|^2|\eta_A(\mathbf{r}')|^2 - \left\{ \eta_A^*(\mathbf{r})\eta_B(\mathbf{r})\eta_B^*(\mathbf{r}')\eta_A(\mathbf{r}')e^{-i[\Phi_A(\mathbf{r})-\Phi_B(\bar{\mathbf{r}})+\Phi_B(\mathbf{r}')-\Phi_A(\bar{\mathbf{r}}')]} + \text{c.c.} \right\}}{[|\eta_A(\mathbf{r})|^2 + |\eta_B(\mathbf{r})|^2][|\eta_A(\mathbf{r}')|^2 + |\eta_B(\mathbf{r}')|^2]}, \quad (20)$$

where $\bar{\mathbf{r}} = \{x, -y, z\}$ characterizes the influence of the reflection operation as shown in Fig. 3(b). For two input photons of the same pulse shape (i.e., $|\eta_A(\mathbf{r})| = |\eta_B(\mathbf{r})|$), the $g^{(2)}$ function reduces to

$$g_{cd}^{(2)}(\mathbf{r}, \mathbf{r}') = \frac{1}{2} \{1 - \cos[\Phi_A(\mathbf{r}) - \Phi_B(\bar{\mathbf{r}}) + \Phi_B(\mathbf{r}') - \Phi_A(\bar{\mathbf{r}}')]\}. \quad (21)$$

The $g^{(2)}$ function of the input product-state photon pairs is a constant 1. The modulation observed in the coherence function, induced by the imposed phases, is entirely attributed to the two-body entanglement generated through HOM interference.

A. Helical continuous phases

The helical phase structure of twisted photons carrying nonvanishing OAM can modify the second-order optical coherence function [41] and lead to interesting HOM interference effects [60,61]. HOM interference of two photons hyperentangled between spin and OAM degrees has also been experimentally demonstrated [62]. Here, we consider a scenario in which helical phases $\Phi_A(\mathbf{r}) = \Phi_B(\mathbf{r}) = m\varphi$ are introduced into the two input channels. No HOM dip or peak will be observed except for $m = 0$ [52] (see more details in the Appendix). However, the azimuthal angles modulate the coherence function $g^{(2)}(\mathbf{r}, \mathbf{r}') = [1 - \cos(2m\varphi + 2m\varphi')]/2$ of the output photons. Our method could also be applied to cases where the OAM quantum numbers of the two input channels are different.

In the experiment [60], Zhang *et al.* demonstrate the HOM dip of entangled twisted photon pairs. By tuning the orientation angle difference φ_0 of a pair of Dove prisms, they added a relative phase ($|m\rangle \rightarrow |m\rangle \exp(i2m\varphi_0)$) between the two entangled photons

$$\xi(\mathbf{r}, \mathbf{r}', t) = \mathcal{N} \eta_m(\mathbf{r}, t) \eta_m(\mathbf{r}', t) \left[e^{im(\varphi+\varphi')} e^{i2m\varphi_0} + \text{c.c.} \right], \quad (22)$$

which can be re-expressed as a superposition of exchange-reflection symmetric and antisymmetric states. The two-port coincidence probability $P_{cd}^{(2)} = [1 - \cos(4m\varphi_0)]/2$ varies with the angle φ_0 and an HOM dip gradually turns to a peak. The entangled twisted photon pair can be exploited for quantum sensing of the rotational angle φ_0 [63] with sensitivity $\propto 2m$. Here, we show that the two-port $g^{(2)}$ function is additionally modulated by the angle φ_0 as well as the two azimuthal angles φ and φ' ,

$$g_{cd}^{(2)}(\mathbf{r}, \mathbf{r}') = \frac{1}{2} \{1 - \cos[2m(\varphi + \varphi')]\}[1 - \cos(4m\varphi_0)]. \quad (23)$$

B. Discontinuous circular-sector phases

The spatially varying phase of photons can provide more powerful ways to control photonic quantum coherence in addition to the helical structure of twisted light. Using a spatial light modulator or a metasurface [27,28], we can imprint arbitrary patterns on the two input photons as shown in previous section. Here, we consider the simplest case where the transverse plane is split into $2m$ (m is an integer) same-sized circular sectors (see Fig. 5).

The spatially varying phases are given by

$$\Phi_A(\varphi) = \begin{cases} \pi, & \varphi \in [(2j-2)\pi/m, (2j-1)\pi/m] \\ 0, & \varphi \in [(2j-1)\pi/m, 2j\pi/m] \end{cases}, \quad (24)$$

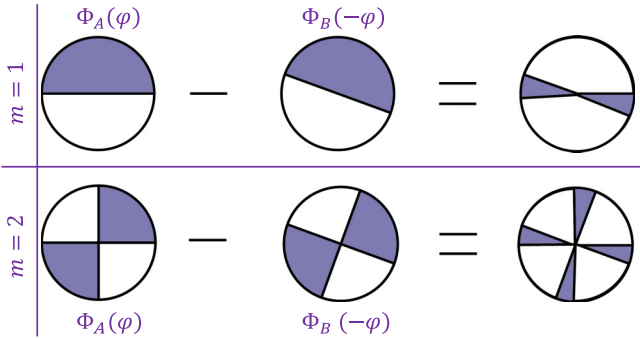


FIG. 5. Phase difference $\Phi_A(\varphi) - \Phi_B(-\varphi)$. (a) The transverse plane is split into two half-circular discs. (b) The transverse plane is split into four equal sectors. The phase of dark regions is π or $-\pi$. The phase of white regions is 0.

and

$$\Phi_B(\varphi)$$

$$= \begin{cases} 0, & \varphi \in [(2j-2)\pi/m + \varphi_0, (2j-1)\pi/m + \varphi_0) \\ \pi, & \varphi \in [(2j-1)\pi/m + \varphi_0, 2j\pi/m + \varphi_0) \end{cases}, \quad (25)$$

where the integer j runs from 1 to m and φ_0 is a mismatch angle of the two phases. The HOM coincidence probability for $\tau = 0$ and $\varphi_0 \in [0, \pi/m]$ is given by

$$P_{cd}^{(2)} = \frac{1}{2} - \frac{1}{4} \int_0^{2\pi} \frac{d\varphi}{2\pi} \times \int_0^{2\pi} \frac{d\varphi'}{2\pi} \left\{ e^{-i[\Phi_A(\varphi) - \Phi_B(-\varphi) + \Phi_B(\varphi') - \Phi_A(-\varphi')]} + e^{-i[\Phi_A(-\varphi) - \Phi_B(\varphi) + \Phi_B(-\varphi') - \Phi_A(\varphi')]} \right\} \quad (26)$$

$$= \frac{1}{2} \left[1 - \left(1 - \frac{m\varphi_0}{\pi} \right)^2 \right], \quad (28)$$

where we have used the normalization condition $\int_0^\infty \rho d\rho \int_{-\infty}^\infty dz |\eta(\mathbf{r}, t)|^2 = 1/2\pi$ and the phase difference shown in Fig. 5.

Our primary focus lies in the manipulation of the detailed coherence function through the engineering of phase profiles in the transverse plane. The photon-number densities at the two output ports are given by $n_c(\mathbf{r}) = |\eta(\mathbf{r})|^2$ and $n_d(\mathbf{r}) = |\eta(\mathbf{r})|^2$, respectively. Similarly, the imposed phases play a role in shaping the second-order coherence function, as described in Eq. (21). Note that

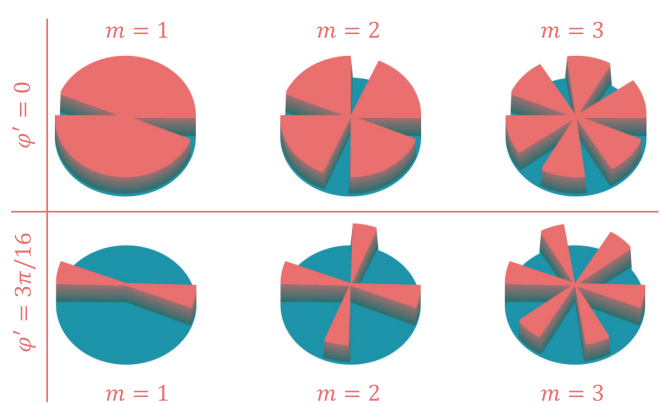


FIG. 6. The $g_{cd}^{(2)}(\mathbf{r}, \mathbf{r}')$ function vary with the azimuthal angle φ . The transverse plane of the two photons has been split into $2m$ same-sized circular sectors with mismatch angle $\varphi_0 = \pi/8$. The azimuthal angle for the top and bottom rows are set as $\varphi' = 0$ and $\varphi' = 3\pi/16$, respectively. The values of the $g^{(2)}$ function in the raised and flat areas are 1 and 0, respectively.

φ changes to $-\varphi$ for $\bar{\mathbf{r}}$. In Fig. 6, we showcase the $g^{(2)}$ function while varying φ and keeping φ' fixed. The mismatch angle is set as $\varphi_0 = \pi/8$. In the top row, \mathbf{r}' is pinned at $\varphi' = 0$. The $g^{(2)}$ function vanishes in regions where $\Phi_A(\varphi) - \Phi_B(-\varphi) = \pm\pi$ as shown in Fig. 5, given that $\Phi_B(\varphi') = 0$ and $\Phi_A(\varphi') = \pi$. In the bottom row, we let $\varphi' = 3\pi/16$. Consequently, the $g^{(2)}$ function vanishes in the complementary regions since $\Phi_B(\varphi') = \Phi_A(-\varphi') = 0$.

Discontinuous jump exists in our simulation of the $g^{(2)}$ function in Fig. 6. However, in experimental settings, a continuous and sharp change would be observed instead. This sharp change presents an opportunity for utilizing the coherence function as a tool for high-sensitivity quantum sensing of the rotational angle φ_0 . By combining this effect with the geometric rotation of photons traveling through a coiled fiber [64–66], the sharp change in the coherence

function of photon pairs can be harnessed for the exploration of another type of laser gyroscope, similar to those based on the Sagnac effect [67].

IV. HIGHER-ORDER COHERENCE CONTROL

Our method can also be extended to control the higher-order coherence of photons. Here, we illustrate only its application using four-photon pulses as an example as depicted in Fig. 7. We begin with a path-entangled four-photon state approximately $(|HH\rangle_1 \otimes |VV\rangle_2 + |VV\rangle_1 \otimes |HH\rangle_2)/\sqrt{2}$. For simplicity, let us consider the case where the four photons share the same shape, characterized by the wave-packet function (WPF) $\eta(\mathbf{r})$, such as a Gaussian profile. Following the two beam splitters, the state of the four photons can be described as

$$|\Psi\rangle = \frac{1}{8\sqrt{2}} \int d\mathbf{r}_1 \int d\mathbf{r}_2 \int d\mathbf{r}_3 \int d\mathbf{r}_4 \eta(\mathbf{r}_1)\eta(\mathbf{r}_2)\eta(\mathbf{r}_3)\eta(\mathbf{r}_4) \left\{ \left[i\hat{\psi}_{A,H}^\dagger(\mathbf{r}_1) + \hat{\psi}_{B,H}^\dagger(\mathbf{r}_1) \right] \left[i\hat{\psi}_{A,H}^\dagger(\mathbf{r}_2) + \hat{\psi}_{B,H}^\dagger(\mathbf{r}_2) \right] \right. \\ \left. + i\hat{\psi}_{C,V}^\dagger(\mathbf{r}_3) + i\hat{\psi}_{D,V}^\dagger(\mathbf{r}_3) \right] \left[i\hat{\psi}_{C,V}^\dagger(\mathbf{r}_4) + i\hat{\psi}_{D,V}^\dagger(\mathbf{r}_4) \right] + (H \leftrightarrow V) \right\} |0\rangle, \quad (29)$$

where the WPF is expressed in four different coordinate frames determined by the propagating axes of the photons and we have used the fact that $\eta(\mathbf{r})$ possesses reflection symmetry, $\eta(\bar{\mathbf{r}}) = \eta(\mathbf{r})$. The field operators satisfy the commutation relation $[\psi_{i,\lambda}(\mathbf{r}), \hat{\psi}_{j,\lambda'}^\dagger(\mathbf{r}')] = \delta_{ij}\delta_{\lambda\lambda'}\delta(\mathbf{r} - \mathbf{r}')$.

Next, we utilize four SLMs to apply distinct phase patterns to the H -polarized photons in the four output channels. The final quantum state $|\tilde{\Psi}\rangle$ of the four photons is obtained by substituting the H -polarization

operator $\psi_{i,H}^\dagger(\mathbf{r})$ ($i = \{A, B, C, D\}$) in Eq. (29) with $\psi_{i,H}^\dagger(\mathbf{r}) \exp[i\Phi_i(\mathbf{r})]$.

The imposed four phases will not change the distribution of photon-number density at each output port

$$n_i(\mathbf{r}) = \sum_\lambda \langle \tilde{\Psi} | \hat{\psi}_{i,\lambda}^\dagger \hat{\psi}_{i,\lambda} | \tilde{\Psi} \rangle = |\eta(\mathbf{r}_i)|^2. \quad (30)$$

We can also evaluate the second- and higher-order correlations of the four-photon state

$$G_{ij}^{(2)}(\mathbf{r}_1, \mathbf{r}_2) = \sum_{\lambda_1 \lambda_2} \langle \tilde{\Psi} | \hat{\psi}_{i,\lambda_1}^\dagger(\mathbf{r}_1) \hat{\psi}_{j,\lambda_2}^\dagger(\mathbf{r}_2) \hat{\psi}_{j,\lambda_2}(\mathbf{r}_2) \hat{\psi}_{i,\lambda_1}(\mathbf{r}_1) | \tilde{\Psi} \rangle, \quad (31)$$

$$= \frac{1}{2} |\eta(\mathbf{r}_1)|^2 |\eta(\mathbf{r}_2)|^2 [\delta_{ij} + \delta_{i,A}\delta_{j,B} + \delta_{i,C}\delta_{j,D} + 2(\delta_{i,A} + \delta_{i,B})(\delta_{j,C} + \delta_{j,D})], \quad (32)$$

$$G_{ijk}^{(3)}(\mathbf{r}_1, \mathbf{r}_2, \mathbf{r}_3) = \sum_{\lambda_1 \lambda_2 \lambda_3} \langle \tilde{\Psi} | \hat{\psi}_{i,\lambda_1}^\dagger(\mathbf{r}_1) \hat{\psi}_{j,\lambda_2}^\dagger(\mathbf{r}_2) \hat{\psi}_{k,\lambda_3}^\dagger(\mathbf{r}_3) \hat{\psi}_{k,\lambda_3}(\mathbf{r}_3) \hat{\psi}_{j,\lambda_2}(\mathbf{r}_2) \hat{\psi}_{i,\lambda_1}(\mathbf{r}_1) | \tilde{\Psi} \rangle, \quad (33)$$

$$= \frac{1}{2} |\eta(\mathbf{r}_1)|^2 |\eta(\mathbf{r}_2)|^2 |\eta(\mathbf{r}_3)|^2 [\delta_{ij}(1 - \delta_{jk})(1 - \delta_{j,A}\delta_{k,B} - \delta_{j,B}\delta_{k,A} - \delta_{j,C}\delta_{k,D} - \delta_{j,D}\delta_{k,C}) + |\epsilon_{ijk}|], \quad (34)$$

$$G_{ijkl}^{(4)}(\mathbf{r}_1, \mathbf{r}_2, \mathbf{r}_3, \mathbf{r}_4) = \sum_{\lambda_1 \lambda_2 \lambda_3 \lambda_4} \langle \tilde{\Psi} | \hat{\psi}_{i,\lambda_1}^\dagger(\mathbf{r}_1) \hat{\psi}_{j,\lambda_2}^\dagger(\mathbf{r}_2) \hat{\psi}_{k,\lambda_3}^\dagger(\mathbf{r}_3) \hat{\psi}_{l,\lambda_4}^\dagger(\mathbf{r}_4) \hat{\psi}_{l,\lambda_4}(\mathbf{r}_4) \hat{\psi}_{k,\lambda_3}(\mathbf{r}_3) \hat{\psi}_{j,\lambda_2}(\mathbf{r}_2) \hat{\psi}_{i,\lambda_1}(\mathbf{r}_1) | \tilde{\Psi} \rangle, \quad (35)$$

$$= \frac{1}{4} |\eta(\mathbf{r}_1)|^2 |\eta(\mathbf{r}_2)|^2 |\eta(\mathbf{r}_3)|^2 |\eta(\mathbf{r}_4)|^2 |\epsilon_{ijkl}|, \quad (36)$$

where ϵ_{ijk} and ϵ_{ijkl} are the Levi-Civita symbols. We observe that the information encoded by the imposed patterned phases cannot be extracted from these correlations. Similar to the two-photon case discussed in Sec. II B, we can obtain the images corresponding to the four patterns from the following fourth-order correlation:

$$G_{ABCD}^{(4)}(\mathbf{r}_1, \mathbf{r}_2, \mathbf{r}_3, \mathbf{r}_4) = \left\langle \tilde{\Psi} \left| \hat{\psi}_{A,L}^\dagger(\mathbf{r}_1) \hat{\psi}_{B,L}^\dagger(\mathbf{r}_2) \hat{\psi}_{C,L}^\dagger(\mathbf{r}_3) \hat{\psi}_{D,L}^\dagger(\mathbf{r}_4) \hat{\psi}_{D,L}(\mathbf{r}_4) \hat{\psi}_{C,L}(\mathbf{r}_3) \hat{\psi}_{B,L}(\mathbf{r}_2) \hat{\psi}_{A,L}(\mathbf{r}_1) \right| \tilde{\Psi} \right\rangle, \quad (37)$$

$$= \frac{1}{64} |\eta(\mathbf{r}_1)|^2 |\eta(\mathbf{r}_2)|^2 |\eta(\mathbf{r}_3)|^2 |\eta(\mathbf{r}_4)|^2 \{1 + \cos[\Phi_A(\mathbf{r}_1) + \Phi_B(\mathbf{r}_2) - \Phi_C(\mathbf{r}_3) - \Phi_D(\mathbf{r}_4)]\}. \quad (38)$$

The $g^{(4)}$ function corresponding to the fourth-order correlation can be obtained as

$$g_{ABCD}^{(4)} = \frac{1}{4} \{1 + \cos[\Phi_A(\mathbf{r}_1) + \Phi_B(\mathbf{r}_2) - \Phi_C(\mathbf{r}_3) - \Phi_D(\mathbf{r}_4)]\}. \quad (39)$$

These patterns encoded in the phases can only be observed in fourth-order correlations.

V. CONCLUSION

We present a theoretical frame showcasing the accurate control of the spatial structure of the quantum coherence function through engineering the phases in their transverse plane. In addition to the helical structure of OAM photons [41], we show that arbitrary patterns of phase profiles can be utilized to tail the coherence function for purposes. Furthermore, our method can be extended to higher-order coherence control. The exceptional controllability of quantum coherence in photons holds the potential for applications such as quantum correlated imaging and quantum sensing of angular rotations. Additionally, it

serves as a driving force for advancing the development of the quantum version of structured illumination microscopy [68,69].

ACKNOWLEDGMENTS

This work is supported by the National Natural Science Foundation of China (Grants No. 12274215, No. 12175033, and No. 12275048); the Program for Innovative Talents and Entrepreneurs in Jiangsu; Key Research and Development Program of Guangdong Province (Grant No. 2020B0303010001).

APPENDIX: COMPREHENSIVE THEORY OF HONG-OU-MANDEL INTERFERENCE

In this Appendix, we present a comprehensive theory of Hong-Ou-Mandel interference involving three-dimensional structured photon pairs and provide several typical examples.

1. Quantum theory of HOM interference for three-dimensional structured photon pairs

This section presents the general theory of HOM interference, which involves the quantum state of a two-photon pulse with polarization degrees of freedom. The state can be expanded using plane-wave modes [41,70]

$$|P_\xi\rangle = \frac{1}{\sqrt{2}} \sum_{\lambda\lambda'} \int d\mathbf{k} \int d\mathbf{k}' \tilde{\xi}_{\lambda\lambda'}(\mathbf{k}, \mathbf{k}') \hat{a}_{\mathbf{k},\lambda}^\dagger(t) \hat{a}_{\mathbf{k}',\lambda'}^\dagger(t) |0\rangle, \quad (A1)$$

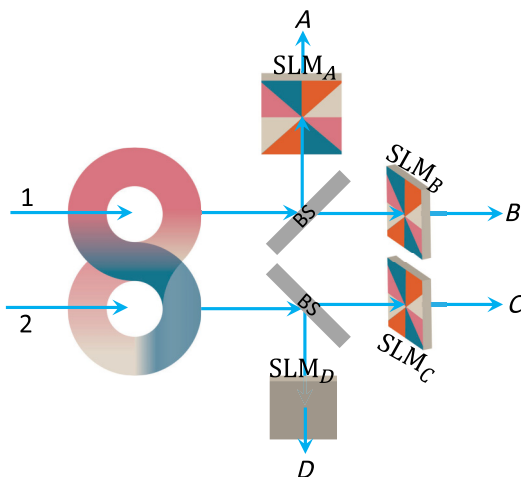


FIG. 7. Fourth-order coherence control scheme. The four photons are initially prepared in an entangled state ($|HH\rangle_1|VV\rangle_2 + |VV\rangle_1|HH\rangle_2$). To generate four output ports, two beam splitters (BSs) are employed. Four SLMs impose four different phase patterns on the four photons.

with creation operators $\hat{a}_{\mathbf{k},\lambda}^\dagger(t) = \hat{a}_{\mathbf{k},\lambda}^\dagger \exp(-i\omega_{\mathbf{k}}t)$ that account for the free time evolution and polarization index λ . The SAF $\tilde{\xi}_{\lambda\lambda'}(\mathbf{k}, \mathbf{k}')$ is normalized $\sum_{\lambda\lambda'} \int d\mathbf{k} \int d\mathbf{k}' |\tilde{\xi}_{\lambda\lambda'}(\mathbf{k}, \mathbf{k}')|^2 = 1$ and the extra factor $1/\sqrt{2}$ results from the bosonic commutation relations $[\hat{a}_{\mathbf{k},\lambda}, \hat{a}_{\mathbf{k}',\lambda'}^\dagger] = \delta_{\lambda\lambda'} \delta(\mathbf{k} - \mathbf{k}')$. The SAF must be symmetric under particle exchange $\{\mathbf{k}, \lambda\} \leftrightarrow \{\mathbf{k}', \lambda'\}$ due to the commutation relations $[\hat{a}_{\mathbf{k},\lambda}, \hat{a}_{\mathbf{k}',\lambda'}] = 0$ and $[\hat{a}_{\mathbf{k},\lambda}^\dagger, \hat{a}_{\mathbf{k}',\lambda'}^\dagger] = 0$. By introducing the effective field operator of photons, the

two-photon state can be re-expressed as [41]

$$|P_\xi\rangle = \frac{1}{\sqrt{2}} \sum_{\lambda\lambda'} \int d\mathbf{r} \int d\mathbf{r}' \xi_{\lambda\lambda'}(\mathbf{r}, \mathbf{r}', t) \hat{\psi}_\lambda^\dagger(\mathbf{r}) \hat{\psi}_{\lambda'}^\dagger(\mathbf{r}') |0\rangle, \quad (\text{A2})$$

with commutation relation $[\hat{\psi}_\lambda(\mathbf{r}), \hat{\psi}_{\lambda'}^\dagger(\mathbf{r}')] = \delta_{\lambda,\lambda'} \delta(\mathbf{r} - \mathbf{r}')$. The real-space WPF

$$\begin{aligned} \xi_{\lambda,\lambda'}(\mathbf{r}, \mathbf{r}', t) &= \frac{1}{(2\pi)^3} \int d\mathbf{k} \\ &\times \int d\mathbf{k}' \tilde{\xi}_{\lambda,\lambda'}(\mathbf{k}, \mathbf{k}') e^{i(\mathbf{k}\cdot\mathbf{r} - \omega_{\mathbf{k}}t + \mathbf{k}'\cdot\mathbf{r}' - \omega_{\mathbf{k}'}t)}, \end{aligned} \quad (\text{A3})$$

is normalized and must also be symmetric under exchange $\{\mathbf{r}, \lambda\} \leftrightarrow \{\mathbf{r}', \lambda'\}$.

Usually, paraxial photon pulses are used in experiments. Two paraxial photons propagating in different directions determined by their center wave vectors as shown in Fig. 8 are spatially distinguishable since there is almost no overlap between WPFs (SAFs) of the two pulses $\xi_{\lambda\lambda'}(\mathbf{r}, \mathbf{r}) \approx 0$ ($\tilde{\xi}_{\lambda\lambda'}(\mathbf{k}, \mathbf{k}) \approx 0$). For convenience, we can employ two coordinate frames with path labels A and B [see Fig. 8(a)] to expand the WPF of each pulse in its respective frame [49]. The two pulses can be approximately treated as two spatially independent modes. Consequently, we can introduce two sets of independent bosonic operators to express

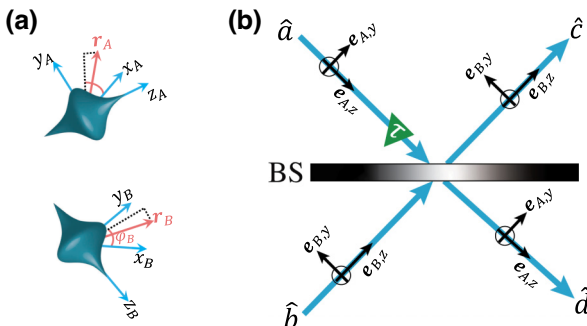


FIG. 8. (a) Two-coordinate-frame formalism. These two coordinates correspond to two propagation paths A and B of the two paraxial photons. The wave-packet functions of the two photons are expressed with coordinates $\mathbf{r}_A = x_A \mathbf{e}_{A,x} + y_A \mathbf{e}_{A,y} + z_A \mathbf{e}_{A,z}$ and $\mathbf{r}_B = x_B \mathbf{e}_{B,x} + y_B \mathbf{e}_{B,y} + z_B \mathbf{e}_{B,z}$, respectively. Two cylindrical coordinate frames have been employed with $x_{A(B)} = \rho_{A(B)} \cos \varphi_{A(B)}$, $y_{A(B)} = \rho_{A(B)} \sin \varphi_{A(B)}$, and $\rho_{A(B)} = \sqrt{x_{A(B)}^2 + y_{A(B)}^2}$. (b) Input-output relations between ladder operators at a BS. The bosonic modes at the input ports are represented by the annihilation operators \hat{a} and \hat{b} . The bosonic modes at the output ports are represented by annihilation operators \hat{c} and \hat{d} . A time delay τ is introduced to generate the Hong-Ou-Mandel dip or peak.

the quantum state of two-photon pulses [52]

$$|P_\xi\rangle = \sum_{\lambda\lambda'} \int d\mathbf{k}_A \int d\mathbf{k}'_B \tilde{\xi}_{\lambda\lambda'}(\mathbf{k}_A, \mathbf{k}'_B) \hat{a}_{\mathbf{k}_A, \lambda}(t) \hat{b}_{\mathbf{k}'_B, \lambda'}^\dagger(t) |0\rangle \quad (\text{A4})$$

$$= \sum_{\lambda\lambda'} \int d\mathbf{r}_A \int d\mathbf{r}'_B \xi_{\lambda\lambda'}(\mathbf{r}_A, \mathbf{r}'_B, t) \hat{\psi}_{a,\lambda}^\dagger(\mathbf{r}_A) \hat{\psi}_{b,\lambda'}^\dagger(\mathbf{r}'_B) |0\rangle. \quad (\text{A5})$$

Here, the ladder (field) operators of two photons commute with each other, i.e., $[\hat{a}_{\mathbf{k}_A, \lambda}, \hat{b}_{\mathbf{k}'_B, \lambda'}^\dagger] = 0$ and $[\hat{\psi}_{a,\lambda}(\mathbf{r}_A), \hat{\psi}_{b,\lambda'}^\dagger(\mathbf{r}'_B)] = 0$ and the factor $1/\sqrt{2}$ in Eq. (A3) is removed. In this representation, the SAF $\tilde{\xi}_{\lambda\lambda'}(\mathbf{k}_A, \mathbf{k}'_B)$ and the real-space WPF $\xi_{\lambda\lambda'}(\mathbf{r}_A, \mathbf{r}'_B, t)$ are not required to be exchange-symmetric any more. This enables the generation of photon pairs with both exchange symmetric and antisymmetric WPFs [49, 62, 70].

The principle of identity plays an essential role in HOM interference when two single-photon pulses meet at a beam splitter [see Fig. 8(b)]. The will be a large overlap between the WPFs of two photons in this case. The effect of indistinguishability manifests in the input-output relations for a beam splitter [49, 52],

$$\hat{c}_{\mathbf{k}_B, \lambda} = (R_{\mathbf{k}} \hat{a}_{\mathbf{k}_A, \lambda} + T_{\mathbf{k}} \hat{b}_{\mathbf{k}_B, \lambda}), \quad (\text{A6})$$

$$\hat{d}_{\mathbf{k}_A, \lambda} = (T_{\mathbf{k}} \hat{a}_{\mathbf{k}_A, \lambda} + R_{\mathbf{k}} \hat{b}_{\mathbf{k}_B, \lambda}), \quad (\text{A7})$$

with $\bar{\mathbf{k}} = (k_x, -k_y, k_z)$ (see the Supplemental Material of Ref. [52]). During an HOM interference, two plane-wave modes $\hat{a}_{\mathbf{k}_A, \lambda}$ and $\hat{b}_{\mathbf{k}_B, \lambda}$ from different input channels could be transformed into modes $\hat{d}_{\mathbf{k}_A, \lambda}$ and $\hat{d}_{\bar{\mathbf{k}}_A, \lambda}$ in the same output channel. The commutation relation between the transmitted and the reflected photon modes at the same output port is given by $[\hat{d}_{\mathbf{k}_A, \lambda}, \hat{d}_{\bar{\mathbf{k}}_A, \lambda}^\dagger] = \delta(\mathbf{k}_A - \bar{\mathbf{k}}_A)$. This implies that the principle of identity ensures that one cannot distinguish between reflected and transmitted photons in a pulse at the same output port. The operators of two different output modes commute. Photons in different output channels are still distinguishable. In the two-coordinate-frame formalism, the y component of wave vector changes sign after a reflection [49, 52]. This leads to a significant effect that the sign of the quantum number of photonic OAM is inverted (i.e., $m \rightarrow -m$) in each reflection [71].

In the HOM interference of a paraxial photon pair, both the reflection and transmission coefficients can be approximately taken as \mathbf{k} -independent constants $T_k = 1/\sqrt{2}$ and $R_k = i/\sqrt{2}$. The output state after HOM interference is given by

$$|\Psi_{\text{out}}\rangle = \frac{1}{2} \sum_{\lambda, \lambda'} \left[i \int d\mathbf{k}_A \int d\mathbf{k}'_A \tilde{\xi}_{\lambda, \lambda'}(\mathbf{k}_A, \mathbf{k}'_A) \hat{d}_{\mathbf{k}_A, \lambda}(t) \hat{d}^\dagger_{\mathbf{k}'_A, \lambda'}(t) + i \int d\mathbf{k}_B \int d\mathbf{k}'_B \tilde{\xi}_{\lambda, \lambda'}(\mathbf{k}_B, \mathbf{k}'_B) \hat{c}_{\mathbf{k}_B, \lambda}(t) \hat{c}^\dagger_{\mathbf{k}'_B, \lambda'}(t) \right. \\ \left. + \int d\mathbf{k}_A \int d\mathbf{k}'_B \tilde{\xi}_{\lambda, \lambda'}(\mathbf{k}_A, \mathbf{k}'_B) \hat{d}_{\mathbf{k}_A, \lambda}(t) \hat{c}^\dagger_{\mathbf{k}'_B, \lambda'}(t) - \int d\mathbf{k}_B \int d\mathbf{k}'_A \tilde{\xi}_{\lambda, \lambda'}(\mathbf{k}_B, \mathbf{k}'_A) \hat{d}^\dagger_{\mathbf{k}'_A, \lambda'}(t) \hat{c}_{\mathbf{k}_B, \lambda}(t) \right] |0\rangle, \quad (\text{A8})$$

$$= \frac{1}{2} \sum_{\lambda, \lambda'} \left[i \int d\mathbf{r}_A \int d\mathbf{r}'_A \tilde{\xi}_{\lambda, \lambda'}(\mathbf{r}_A, \mathbf{r}'_A, t) \hat{\psi}_{d, \lambda}^\dagger(\mathbf{r}_A) \hat{\psi}_{d, \lambda'}^\dagger(\mathbf{r}'_A) + i \int d\mathbf{r}_B \int d\mathbf{r}'_B \tilde{\xi}_{\lambda, \lambda'}(\mathbf{r}_B, \mathbf{r}'_B, t) \hat{\psi}_{c, \lambda}^\dagger(\mathbf{r}_B) \hat{\psi}_{c, \lambda'}^\dagger(\mathbf{r}'_B) \right. \\ \left. + \int d\mathbf{r}_A \int d\mathbf{r}'_B \tilde{\xi}_{cd}(\mathbf{r}_A, \mathbf{r}'_B, t) \hat{\psi}_{d, \lambda}^\dagger(\mathbf{r}_A) \hat{\psi}_{c, \lambda'}^\dagger(\mathbf{r}'_B) \right] |0\rangle, \quad (\text{A9})$$

with $\bar{\mathbf{r}} = (x, -y, z)$ and WPF

$$\xi_{cd}(\mathbf{r}_A, \mathbf{r}'_B, t) = \xi_{\lambda, \lambda'}(\mathbf{r}_A, \mathbf{r}'_B, t) - \xi_{\lambda', \lambda}(\bar{\mathbf{r}}'_B, \bar{\mathbf{r}}_A, t). \quad (\text{A10})$$

The first two terms in state $|\Psi_{\text{out}}\rangle$ represent photons coming out from the same port of the beam splitter—bunching photons. The third term represents the two photons coming out of different ports—antibunching photons.

We emphasize that the HOM interference is not solely determined by the exchange symmetry of a photon pair, but the combined exchange-reflection symmetry. We introduce a symmetry index $s = \pm 1$ for the exchange-reflection symmetry condition $\xi_{\lambda, \lambda'}(\mathbf{r}_A, \mathbf{r}'_B, t) = s \xi_{\lambda', \lambda}(\bar{\mathbf{r}}'_B, \bar{\mathbf{r}}_A, t)$. Destructive (dip) and constructive (peak) HOM interferences are obtained with $s = +1$ and $s = -1$, respectively.

In experiments, the two-photon coincidence probability

$$P_{cd}^{(2)} = \langle \Psi_{\text{out}} | \hat{N}_c \otimes \hat{N}_d | \Psi_{\text{out}} \rangle, \quad (\text{A11})$$

has been used to demonstrate the HOM interference. For single-photon detectors with flat frequency response, the measurements at two output ports can be described by paraxial photon-number operators [41, 72]

$$\hat{N}_c = \int d\mathbf{k}_B \hat{c}_{\mathbf{k}_B, \lambda}^\dagger \hat{c}_{\mathbf{k}_B, \lambda} = \int d\mathbf{r}_B \hat{\psi}_{c, \lambda}^\dagger(\mathbf{r}_B) \hat{\psi}_{c, \lambda}(\mathbf{r}_B), \quad (\text{A12})$$

$$\hat{N}_d = \int d\mathbf{k}_A \hat{d}_{\mathbf{k}_A, \lambda}^\dagger \hat{d}_{\mathbf{k}_A, \lambda} = \int d\mathbf{r}_A \hat{\psi}_{d, \lambda}^\dagger(\mathbf{r}_A) \hat{\psi}_{d, \lambda}(\mathbf{r}_A). \quad (\text{A13})$$

From Eqs. (A11)–(A13), we obtain the coincidence probability

$$P_{cd}^{(2)} = \frac{1}{2} - \frac{1}{4} \sum_{\lambda, \lambda'} \int d\mathbf{k}_A \int d\mathbf{k}'_B \left[\tilde{\xi}_{\lambda, \lambda'}^*(\mathbf{k}_A, \mathbf{k}'_B) \tilde{\xi}_{\lambda', \lambda}(\bar{\mathbf{k}}'_B, \bar{\mathbf{k}}_A) + \tilde{\xi}_{\lambda', \lambda}^*(\bar{\mathbf{k}}'_B, \bar{\mathbf{k}}_A) \tilde{\xi}_{\lambda, \lambda'}(\mathbf{k}_A, \mathbf{k}'_B) \right], \quad (\text{A14})$$

$$= \frac{1}{2} - \frac{1}{4} \sum_{\lambda, \lambda'} \int d\mathbf{r}_A \int d\mathbf{r}'_B \left[\xi_{\lambda, \lambda'}^*(\mathbf{r}_A, \mathbf{r}'_B, t) \xi_{\lambda', \lambda}(\bar{\mathbf{r}}'_B, \bar{\mathbf{r}}_A, t) + \xi_{\lambda', \lambda}^*(\bar{\mathbf{r}}'_B, \bar{\mathbf{r}}_A, t) \xi_{\lambda, \lambda'}(\mathbf{r}_A, \mathbf{r}'_B, t) \right]. \quad (\text{A15})$$

A similar theory has been presented in the prior literature [50], which has also been extended to mixed states [51]. In the subsequent sections, we provide a comprehensive analysis of the distinguishability of spatiotemporal and polarization properties in HOM interference using OAM or polarization-entangled photon pairs. This analysis serves as inspiration for the development of precise methods to manipulate the higher-order coherence of entangled photons in the main text.

2. Spatiotemporal distinguishability

Here we study how the spatiotemporal distinguishability of the input photons influences the HOM coincidence

measurements. Specifically, we investigate the role of the helical structure of linearly polarized twisted photon pairs in HOM interference. In this subsection, we neglect the polarization indices for simplicity.

a. Product-state twisted photon pair

We first consider two input photons in a product state with an SAF

$$\tilde{\eta}(\mathbf{k}, \mathbf{k}') = \mathcal{N} \tilde{\eta}(\mathbf{k}) \tilde{\eta}(\mathbf{k}') e^{i[m(\tilde{\varphi} - \tilde{\varphi}')] } e^{-ik_z z_0}, \quad (\text{A16})$$

where the normalization factor is $\mathcal{N} = 1$ and $\tilde{\varphi}$ ($\tilde{\varphi}'$) is the azimuthal angle of the wave vector \mathbf{k} (\mathbf{k}') in the

momentum-space cylindrical coordinate. The integer m represents the OAM quantum number of each photon, and the normalized function $\tilde{\eta}(\mathbf{k})$ characterizes the pulse shape and pulse length of the two photons and is usually independent on azimuthal angle $\tilde{\varphi}$ [41, 52]. To simplify, we will omit the path labels A and B unless they are necessary. We note that two photons in this pulse have opposite OAM quantum numbers. The corresponding WPF is given by

$$\xi(\mathbf{r}, \mathbf{r}', t) = \mathcal{N} \eta_m(\mathbf{r}, t + \tau) \eta_{-m}(\mathbf{r}', t) e^{im(\varphi - \varphi')}, \quad (\text{A17})$$

with

$$\eta_{\pm m}(\mathbf{r}, t) = \frac{i^{\pm m}}{\sqrt{2\pi}} \int_{-\infty}^{\infty} dk_z \times \int_0^{\infty} \tilde{\rho} d\tilde{\rho} \tilde{\eta}(k_z, \tilde{\rho}) J_{\pm m}(\rho \tilde{\rho}) e^{i(k_z z - \omega_{\mathbf{k}} t)}, \quad (\text{A18})$$

where $\rho = \sqrt{x^2 + y^2}$ and $\tilde{\rho} = \sqrt{k_x^2 + k_y^2}$ represent the magnitudes of the vector projections of \mathbf{r} and \mathbf{k} onto the x - y plane, respectively, and $J_n(x)$ is the n th-order Bessel function of the first kind. We have used the fact that $J_m(x) = (-1)^m J_{-m}(x)$ and in the last step. We note that the function $\eta_m(\mathbf{r}, t)$ is independent on the azimuthal angle φ and $\eta_m(\mathbf{r}, t) = \eta_{-m}(\mathbf{r}, t)$ [52]. A time delay $\tau = z_0/c$ is added in path A [see Fig. 8(b)].

The coincidence probability after the BS is obtained from Eq. (A11) as

$$P_{cd}^{(2)} = \frac{1}{2} - \frac{1}{2} \int d\mathbf{k} \int d\mathbf{k}' |\tilde{\eta}(\mathbf{k})|^2 |\tilde{\eta}(\mathbf{k}')|^2 e^{i(k_z - k'_z)z_0}. \quad (\text{A19})$$

In the absence of delay (i.e., $\tau = z_0/c = 0$), one can easily verify that the WPF in Eq. (A17) satisfies the exchange-reflection condition $\xi(\bar{\mathbf{r}}, \bar{\mathbf{r}}, t) = \xi(\mathbf{r}, \mathbf{r}', t)$ (note the sign change in m by $\bar{\mathbf{r}}$ [52]). No coincidence events will be observed in experiments. An HOM interference dip will be obtained by varying the optical path (i.e., the delay τ) in one of the input ports as shown by the pink dotted line in Fig. 9(a).

We now consider two photons with the same OAM quantum number. The SAF of the photon pair

$$\tilde{\xi}(\mathbf{k}, \mathbf{k}') = \mathcal{N} \tilde{\eta}(\mathbf{k}) \tilde{\eta}(\mathbf{k}') e^{i[m(\tilde{\varphi} + \tilde{\varphi}')] z_0}, \quad (\text{A20})$$

is exchange symmetric in the absence of a delay (i.e., $z_0 = 0$). However, the corresponding WPF

$$\xi(\mathbf{r}, \mathbf{r}', t) = \mathcal{N} \eta_m(\mathbf{r}, t + \tau) \eta_m(\mathbf{r}', t) e^{im(\varphi + \varphi')}, \quad (\text{A21})$$

does not have the exchange-reflection symmetry except for $m = 0$ [52], i.e., $\xi(\bar{\mathbf{r}}, \bar{\mathbf{r}}, t) \neq \pm \xi(\mathbf{r}, \mathbf{r}', t)$. After the HOM

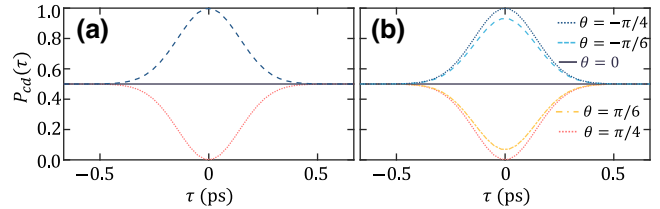


FIG. 9. Coincidence probability in HOM interference. (a) Control the HOM interference via orbital-angular-momentum degrees of photons. The pink dotted line corresponds to twisted photon pairs with SAF given in Eqs. (A16), (A23), and (A29). The black solid line corresponds to a photon pair with SAF given in Eq. (A20). The navy-blue dashed line corresponds to a twisted photon pair with SAF given in Eq. (A26). (b) Control the HOM interference via polarization degrees of photons. The curves from top to bottom correspond to $\theta = -\pi/4, -\pi/6, 0, \pi/6, \pi/4$, respectively. Here, the size of the pulse is set to 3×10^{-5} m (corresponding to the pulse length in time 10^{-13} s).

interference, the coincidence probability is given by

$$P_{cd}^{(2)} = \frac{1}{2} - \frac{1}{2} \int d\mathbf{k} \int d\mathbf{k}' \mathcal{N}^2 |\tilde{\eta}(\mathbf{k})|^2 |\tilde{\eta}(\mathbf{k}')|^2 \times \cos[2m(\tilde{\varphi} + \tilde{\varphi}')] e^{i(k_z - k'_z)z_0}. \quad (\text{A22})$$

We can further verify that $P_{cd}^{(2)} = (1 - \delta_{m,0})/2$ for $z_0 = 0$. As shown by the black solid line in Fig. 9(a), the HOM dip vanishes for nonzero OAM quantum number ($m \neq 0$). Here, we clearly show that not the exchange symmetry but the combined exchange-reflection symmetry plays an essential role in HOM interference.

b. Entangled twisted photon pair

Next, we study the HOM interference of entangled twisted photon pairs, which have been extensively used in quantum communications and quantum sensing experiments. We first consider a twisted photon pair with an exchange symmetric SAF in the absence of a delay

$$\tilde{\xi}(\mathbf{k}, \mathbf{k}') = \mathcal{N} \tilde{\eta}(\mathbf{k}) \tilde{\eta}(\mathbf{k}') \left[e^{im(\tilde{\varphi} + \tilde{\varphi}')} + e^{-im(\tilde{\varphi} + \tilde{\varphi}')} \right] e^{-ik_z z_0}, \quad (\text{A23})$$

where the two photons always have the same OAM quantum number and $\mathcal{N} = [2(1 + \delta_{m,0})]^{-1/2}$. The corresponding WPF

$$\xi(\mathbf{r}, \mathbf{r}', t) = \mathcal{N} \eta_m(\mathbf{r}, t + \tau) \eta_m(\mathbf{r}', t) \left[e^{im(\varphi + \varphi')} + e^{-im(\varphi + \varphi')} \right], \quad (\text{A24})$$

satisfies the exchange-reflection symmetry condition $\xi(\bar{\mathbf{r}}', \bar{\mathbf{r}}, t) = \xi(\mathbf{r}, \mathbf{r}', t)$ for $\tau = 0$. The coincidence probability is given by

$$P_{cd}^{(2)} = \frac{1}{2} - \frac{1}{2} \int d\mathbf{k} \int d\mathbf{k}' \mathcal{N}^2 |\tilde{\eta}(\mathbf{k})|^2 |\tilde{\eta}(\mathbf{k}')|^2 \times (2 + 2 \cos [2m(\tilde{\varphi} + \tilde{\varphi}')] e^{i(k_z - k'_z)z_0}). \quad (\text{A25})$$

The coincidence probability vanishes $P_{cd}^{(2)} = 0$ for $z_0 = 0$. This implies that an HOM dip will be obtained as shown by the pink dotted line in Fig. 9(a).

We now consider another entangled twisted photon pair with exchange symmetric SAF in the absence of delay

$$\tilde{\xi}(\mathbf{k}, \mathbf{k}') = \mathcal{N} \tilde{\eta}(\mathbf{k}) \tilde{\eta}(\mathbf{k}') \left[e^{im(\tilde{\varphi} + \tilde{\varphi}')} - e^{-im(\tilde{\varphi} + \tilde{\varphi}')} \right] e^{-ik_z z_0}, \quad (\text{A26})$$

where $\mathcal{N} = 1/\sqrt{2}$ ($m \neq 0$). However, the corresponding WPF

$$\xi(\mathbf{r}, \mathbf{r}', t) = \mathcal{N} \eta_m(\mathbf{r}, t + \tau) \eta_m(\mathbf{r}', t) \left[e^{im(\varphi + \varphi')} - e^{-im(\varphi + \varphi')} \right], \quad (\text{A27})$$

is exchange-reflection anti-symmetric $\xi(\bar{\mathbf{r}}', \bar{\mathbf{r}}, t) = -\xi(\mathbf{r}, \mathbf{r}', t)$ for $\tau = z_0/c = 0$ [52]. The corresponding coincidence probability is obtained as

$$P_{cd}^{(2)} = \frac{1}{2} + \frac{1}{2} \int d\mathbf{k} \int d\mathbf{k}' \mathcal{N}^2 |\tilde{\eta}(\mathbf{k})|^2 |\tilde{\eta}(\mathbf{k}')|^2 \times (2 - 2 \cos [2m(\tilde{\varphi} + \tilde{\varphi}')] e^{i(k_z - k'_z)z_0}). \quad (\text{A28})$$

In this case, an HOM peak will be obtained as shown by the navy-blue dashed line in Fig. 9(a).

If two photons carry an equal amount of OAM but with the opposite sign, we can have entangled photon pairs with SAF

$$\tilde{\xi}^\pm(\mathbf{k}, \mathbf{k}') = \mathcal{N} \tilde{\eta}(\mathbf{k}) \tilde{\eta}(\mathbf{k}') \left[e^{im(\tilde{\varphi} - \tilde{\varphi}')} \pm e^{-im(\tilde{\varphi} - \tilde{\varphi}')} \right] e^{-ik_z z_0}. \quad (\text{A29})$$

In the absence of delay, the SAF $\tilde{\xi}^+(\mathbf{k}, \mathbf{k}')$ and $\tilde{\xi}^-(\mathbf{k}, \mathbf{k}')$ are exchange symmetric and antisymmetric, respectively. However, the corresponding two WPFs

$$\xi^\pm(\mathbf{r}, \mathbf{r}', t) = \mathcal{N} \eta_m(\mathbf{r}, t + \tau) \eta_m(\mathbf{r}', t) \left[e^{im(\varphi - \varphi')} \pm e^{-im(\varphi - \varphi')} \right], \quad (\text{A30})$$

both satisfy the exchange-reflection symmetric condition $\xi^\pm(\bar{\mathbf{r}}', \bar{\mathbf{r}}, t) = \xi^\pm(\mathbf{r}, \mathbf{r}', t)$ when $\tau = 0$. The coincidence

probability is given by

$$P_{cd,\pm}^{(2)} = \frac{1}{2} - \frac{1}{2} \int d\mathbf{k} \int d\mathbf{k}' \mathcal{N}^2 |\tilde{\eta}(\mathbf{k})|^2 |\tilde{\eta}(\mathbf{k}')|^2 \times (2 \pm 2 \cos [2m(\tilde{\varphi} - \tilde{\varphi}')] e^{i(k_z - k'_z)z_0}). \quad (\text{A31})$$

Only an HOM dip will be obtained for both the exchange symmetric and antisymmetric photon pairs as shown by the pink dotted line in Fig. 9(a).

3. Polarization distinguishability

In this subsection, we consider the influences of polarization distinguishability on two-photon HOM coincidence measurements. We apply our theory to a photon pair with entangled polarization states

$$\tilde{\xi}_{\lambda\lambda'}(\mathbf{k}, \mathbf{k}') = \frac{1}{\sqrt{2}} \tilde{\xi}(\mathbf{k}, \mathbf{k}') \left[\delta_{\lambda,H} \delta_{\lambda',V} \cos \theta + \delta_{\lambda,V} \delta_{\lambda',H} \sin \theta \right], \quad (\text{A32})$$

where H (V) denotes the horizontal (vertical) polarization and θ is the mixing angle between states $|HV\rangle$ and $|VH\rangle$. We can take the SAF $\tilde{\xi}(\mathbf{k}, \mathbf{k}')$ being of the product of two Gaussian functions, which is exchange-reflection symmetric without delay.

The coincidence probability

$$P_{cd}^{(2)} = \frac{1}{2} - \frac{1}{4} \sin 2\theta \int d\mathbf{k} \int d\mathbf{k}' \left[\tilde{\xi}^*(\mathbf{k}, \mathbf{k}') \tilde{\xi}(\bar{\mathbf{k}}, \bar{\mathbf{k}}) + \text{h.c.} \right], \quad (\text{A33})$$

can be continuously tuned by varying the mixing angle θ as shown in Fig. 9(b). For $\theta = -\pi/4$, the polarization of the photon pair is described by state $(|HV\rangle - |VH\rangle)/\sqrt{2}$, which is exchange antisymmetric. Different from the OAM degrees of freedom, the polarization of photons does not change at the beam splitter. Therefore, the total WPF is exchange-reflection antisymmetric and an HOM peak is obtained. Similarly, an HOM dip is obtained for $\theta = \pi/4$, since the corresponding polarization state $(|HV\rangle + |VH\rangle)/\sqrt{2}$ is exchange symmetric. For $\theta = 0$, the polarization of the photon pair is $|HV\rangle$. The two photons are distinguishable via their polarizations. Thus, no HOM interference will be observed as shown by the black solid line in Fig. 9(b). The coincidence contrast decreases to zero by varying $|\theta|$ from $\pi/4$ to 0. Recently, Liu *et al.* experimentally studied 16 polarization-OAM hyperentangled two-photon states [62]. In Appendix A 4, we compared our theoretical results with this experiment. Our theory is consistent with their results.

4. Comparison with the previous experiment

In Table I, we compare our theoretical results with the experiment [62]. We note that the notation of the two-photon states in Ref. [62] is different from this work. The

TABLE I. Comparison of experiment and our theoretical results for HOM interference of sixteen hyperentangled Bell states.

State in Ref. [62]	State at the beam splitter	s	Experiment	Theory
$ \phi^+\rangle_{12} \otimes \mu^+\rangle_{12}$	$(H\rangle_1 H\rangle_2 + V\rangle_1 V\rangle_2) \otimes (+m\rangle_1 m\rangle_2 + -m\rangle_1+m\rangle_2)/2$	+1	dip	dip
$ \phi^+\rangle_{12} \otimes \mu^-\rangle_{12}$	$(H\rangle_1 H\rangle_2 + V\rangle_1 V\rangle_2) \otimes (+m\rangle_1 m\rangle_2 - -m\rangle_1+m\rangle_2)/2$	+1	dip	dip
$ \phi^+\rangle_{12} \otimes \nu^+\rangle_{12}$	$(H\rangle_1 H\rangle_2 + V\rangle_1 V\rangle_2) \otimes (+m\rangle_1+m\rangle_2 + -m\rangle_1-m\rangle_2)/2$	+1	dip	dip
$ \phi^+\rangle_{12} \otimes \nu^-\rangle_{12}$	$(H\rangle_1 H\rangle_2 + V\rangle_1 V\rangle_2) \otimes (+m\rangle_1+m\rangle_2 - -m\rangle_1-m\rangle_2)/2$	-1	peak	peak
$ \phi^-\rangle_{12} \otimes \mu^+\rangle_{12}$	$(H\rangle_1 H\rangle_2 - V\rangle_1 V\rangle_2) \otimes (+m\rangle_1 m\rangle_2 + -m\rangle_1+m\rangle_2)/2$	+1	dip	dip
$ \phi^-\rangle_{12} \otimes \mu^-\rangle_{12}$	$(H\rangle_1 H\rangle_2 - V\rangle_1 V\rangle_2) \otimes (+m\rangle_1 m\rangle_2 - -m\rangle_1+m\rangle_2)/2$	+1	dip	dip
$ \phi^-\rangle_{12} \otimes \nu^+\rangle_{12}$	$(H\rangle_1 H\rangle_2 - V\rangle_1 V\rangle_2) \otimes (+m\rangle_1+m\rangle_2 + -m\rangle_1-m\rangle_2)/2$	+1	dip	dip
$ \phi^-\rangle_{12} \otimes \nu^-\rangle_{12}$	$(H\rangle_1 H\rangle_2 - V\rangle_1 V\rangle_2) \otimes (+m\rangle_1+m\rangle_2 - -m\rangle_1-m\rangle_2)/2$	-1	peak	peak
$ \psi^+\rangle_{12} \otimes \mu^+\rangle_{12}$	$(H\rangle_1 V\rangle_2 + V\rangle_1 H\rangle_2) \otimes (+m\rangle_1 m\rangle_2 + -m\rangle_1+m\rangle_2)/2$	+1	dip	dip
$ \psi^+\rangle_{12} \otimes \mu^-\rangle_{12}$	$(H\rangle_1 V\rangle_2 + V\rangle_1 H\rangle_2) \otimes (+m\rangle_1 m\rangle_2 - -m\rangle_1+m\rangle_2)/2$	+1	dip	dip
$ \psi^+\rangle_{12} \otimes \nu^+\rangle_{12}$	$(H\rangle_1 V\rangle_2 + V\rangle_1 H\rangle_2) \otimes (+m\rangle_1+m\rangle_2 + -m\rangle_1-m\rangle_2)/2$	+1	dip	dip
$ \psi^+\rangle_{12} \otimes \nu^-\rangle_{12}$	$(H\rangle_1 V\rangle_2 + V\rangle_1 H\rangle_2) \otimes (+m\rangle_1+m\rangle_2 - -m\rangle_1-m\rangle_2)/2$	+1	peak	peak
$ \psi^-\rangle_{12} \otimes \mu^+\rangle_{12}$	$(H\rangle_1 V\rangle_2 - V\rangle_1 H\rangle_2) \otimes (+m\rangle_1 m\rangle_2 + -m\rangle_1+m\rangle_2)/2$	-1	peak	peak
$ \psi^-\rangle_{12} \otimes \mu^-\rangle_{12}$	$(H\rangle_1 V\rangle_2 - V\rangle_1 H\rangle_2) \otimes (+m\rangle_1 m\rangle_2 - -m\rangle_1+m\rangle_2)/2$	-1	peak	peak
$ \psi^-\rangle_{12} \otimes \nu^+\rangle_{12}$	$(H\rangle_1 V\rangle_2 - V\rangle_1 H\rangle_2) \otimes (+m\rangle_1+m\rangle_2 + -m\rangle_1-m\rangle_2)/2$	-1	peak	peak
$ \psi^-\rangle_{12} \otimes \nu^-\rangle_{12}$	$(H\rangle_1 V\rangle_2 - V\rangle_1 H\rangle_2) \otimes (+m\rangle_1+m\rangle_2 - -m\rangle_1-m\rangle_2)/2$	+1	dip	dip

times of reflection for the two optical paths are different. Thus, the true quantum states of the 16 two-photon pulses at the beam splitter are given by the second column of Table I. From the output state (A9), we see that the destructive or constructive HOM interference is determined by $\xi_{\lambda,\lambda'}(\mathbf{r}, \mathbf{r}', t) = s\xi_{\lambda',\lambda}(\bar{\mathbf{r}}', \bar{\mathbf{r}}, t)$ ($s = \pm 1$), not the exchange symmetry of the total wave function directly. The HOM dip and peak are obtained with $s = +1$ and peak $s = -1$, respectively. Our theory is consistent with the experiment [62].

-
- [1] V. Giovannetti, S. Lloyd, and L. Maccone, Quantum-enhanced measurements: Beating the standard quantum limit, *Science* **306**, 1330 (2004).
 - [2] J. P. Dowling, Quantum optical metrology—the lowdown on high-N0ON states, *Contemp. Phys.* **49**, 125 (2008).
 - [3] S. Lloyd, Enhanced sensitivity of photodetection via quantum illumination, *Science* **321**, 1463 (2008).
 - [4] D. F. Walls, Squeezed states of light, *nature* **306**, 141 (1983).
 - [5] L.-A. Wu, H. J. Kimble, J. L. Hall, and H. Wu, Generation of squeezed states by parametric down conversion, *Phys. Rev. Lett.* **57**, 2520 (1986).
 - [6] R. E. Slusher, L. W. Hollberg, B. Yurke, J. C. Mertz, and J. F. Valley, Observation of squeezed states generated by four-wave mixing in an optical cavity, *Phys. Rev. Lett.* **55**, 2409 (1985).
 - [7] P. Kok, H. Lee, and J. P. Dowling, Creation of large-photon-number path entanglement conditioned on photodetection, *Phys. Rev. A* **65**, 052104 (2002).
 - [8] I. Afek, O. Ambar, and Y. Silberberg, High-NOON states by mixing quantum and classical light, *Science* **328**, 879 (2010).
 - [9] P. G. Kwiat, E. Waks, A. G. White, I. Appelbaum, and P. H. Eberhard, Ultrabright source of polarization-entangled photons, *Phys. Rev. A* **60**, R773 (1999).
 - [10] N. Gisin, G. Ribordy, W. Tittel, and H. Zbinden, Quantum cryptography, *Rev. Mod. Phys.* **74**, 145 (2002).
 - [11] R. J. Glauber, The quantum theory of optical coherence, *Phys. Rev.* **130**, 2529 (1963).
 - [12] G. Brida, M. Genovese, and I. R. Berchera, Experimental realization of sub-shot-noise quantum imaging, *Nat. Photonics* **4**, 227 (2010).
 - [13] T. Ono, R. Okamoto, and S. Takeuchi, An entanglement-enhanced microscope, *Nat. Commun.* **4**, 2426 (2013).
 - [14] T. Gregory, P.-A. Moreau, E. Toninelli, and M. J. Padgett, Imaging through noise with quantum illumination, *Sci. Adv.* **6**, eaay2652 (2020).
 - [15] P.-A. Moreau, E. Toninelli, T. Gregory, and M. J. Padgett, Imaging with quantum states of light, *Nat. Rev. Phys.* **1**, 367 (2019).
 - [16] F. Wolfgramm, C. Vitelli, F. A. Beduini, N. Godbout, and M. W. Mitchell, Entanglement-enhanced probing of a delicate material system, *Nat. Photonics* **7**, 28 (2013).
 - [17] Y. Israel, S. Rosen, and Y. Silberberg, Supersensitive polarization microscopy using noon states of light, *Phys. Rev. Lett.* **112**, 103604 (2014).
 - [18] Z. He, Y. Zhang, X. Tong, L. Li, and L. V. Wang, Quantum microscopy of cells at the Heisenberg limit, *Nat. Commun.* **14**, 2441 (2023).
 - [19] H. Defienne, B. Ndagano, A. Lyons, and D. Faccio, Polarization entanglement-enabled quantum holography, *Nat. Phys.* **17**, 591 (2021).
 - [20] R. Camphausen, Álvaro Cuevas, L. Duempelmann, R. A. Terborg, E. Wajs, S. Tisa, A. Ruggeri, I. Cusini, F. Steinlechner, and V. Pruneri, A quantum-enhanced wide-field phase imager, *Sci. Adv.* **7**, eabj2155 (2021).
 - [21] A. N. Black, L. D. Nguyen, B. Braverman, K. T. Crampston, J. E. Evans, and R. W. Boyd, Quantum-enhanced

- phase imaging without coincidence counting, *Optica* **10**, 952 (2023).
- [22] R. Chrapkiewicz, M. Jachura, K. Banaszek, and W. Wasilewski, Hologram of a single photon, *Nat. Photonics* **10**, 576 (2016).
- [23] B. Ndagano, H. Defienne, D. Branford, Y. D. Shah, A. Lyons, N. Westerberg, E. M. Gauger, and D. Faccio, Quantum microscopy based on Hong–Ou–Mandel interference, *Nat. Photonics* **16**, 384 (2022).
- [24] D. Zia, N. Dehghan, A. D’Errico, F. Sciarrino, and E. Karimi, Interferometric imaging of amplitude and phase of spatial biphoton states, *Nat. Photonics* **17**, 1009 (2023).
- [25] S. P. Walborn, C. Monken, S. Pádua, and P. S. Ribeiro, Spatial correlations in parametric down-conversion, *Phys. Rep.* **495**, 87 (2010).
- [26] C. K. Law and J. H. Eberly, Analysis and interpretation of high transverse entanglement in optical parametric down conversion, *Phys. Rev. Lett.* **92**, 127903 (2004).
- [27] N. Yu, P. Genevet, M. A. Kats, F. Aieta, J.-P. Tetienne, F. Capasso, and Z. Gaburro, Light propagation with phase discontinuities: Generalized laws of reflection and refraction, *Science* **334**, 333 (2011).
- [28] R. C. Devlin, A. Ambrosio, N. A. Rubin, J. P. B. Mueller, and F. Capasso, Arbitrary spin-to-orbital angular momentum conversion of light, *Science* **358**, 896 (2017).
- [29] Y. Shen, X. Wang, Z. Xie, C. Min, X. Fu, Q. Liu, M. Gong, and X. Yuan, Optical vortices 30 years on: OAM manipulation from topological charge to multiple singularities, *Light Sci. Appl.* **8**, 90 (2019).
- [30] A. Forbes, Structured light: Tailored for purpose, *Opt. Photon. News* **31**, 24 (2020).
- [31] E. Nagali, F. Sciarrino, F. De Martini, L. Marrucci, B. Piccirillo, E. Karimi, and E. Santamato, Quantum information transfer from spin to orbital angular momentum of photons, *Phys. Rev. Lett.* **103**, 013601 (2009).
- [32] T. Stav, A. Faerman, E. Maguid, D. Oren, V. Kleiner, E. Hasman, and M. Segev, Quantum entanglement of the spin and orbital angular momentum of photons using metamaterials, *Science* **361**, 1101 (2018).
- [33] C.-Y. Li, S.-J. Liu, B.-S. Yu, H.-J. Wu, C. Rosales-Guzmán, Y. Shen, P. Chen, Z.-H. Zhu, and Y.-Q. Lu, Toward arbitrary spin-orbit flat optics via structured geometric phase gratings, *Laser. Photon. Rev.* **17**, 2200800 (2023).
- [34] P. A. Morris, R. S. Aspden, J. E. Bell, R. W. Boyd, and M. J. Padgett, Imaging with a small number of photons, *Nat. Commun.* **6**, 1 (2015).
- [35] G. B. Lemos, V. Borish, G. D. Cole, S. Ramelow, R. Lapkiewicz, and A. Zeilinger, Quantum imaging with undetected photons, *Nature* **512**, 409 (2014).
- [36] O. S. Magaña-Loaiza and R. W. Boyd, Quantum imaging and information, *Rep. Prog. Phys.* **82**, 124401 (2019).
- [37] M. P. J. Lavery, F. C. Speirsits, S. M. Barnett, and M. J. Padgett, Detection of a spinning object using light’s orbital angular momentum, *Science* **341**, 537 (2013).
- [38] O. Korech, U. Steinitz, R. J. Gordon, I. S. Averbukh, and Y. Prior, Observing molecular spinning via the rotational Doppler effect, *Nat. Photonics* **7**, 711 (2013).
- [39] W. Zhang, D. Zhang, X. Qiu, and L. Chen, Quantum remote sensing of the angular rotation of structured objects, *Phys. Rev. A* **100**, 043832 (2019).
- [40] S. Qiu, Y. Ding, T. Liu, Z. Liu, H. Wu, and Y. Ren, Fragmental optical vortex for the detection of rotating object based on the rotational doppler effect, *Opt. Express* **30**, 47350 (2022).
- [41] L.-P. Yang and D. Xu, Quantum theory of photonic vortices and quantum statistics of twisted photons, *Phys. Rev. A* **105**, 023723 (2022).
- [42] X. Gao, Y. Zhang, A. D’Errico, A. Sit, K. Heshami, and E. Karimi, Full spatial characterization of entangled structured photons, *ArXiv:2304.14280* (2023).
- [43] S.-Y. Huang, J. Gao, Z.-C. Ren, Z.-M. Cheng, W.-Z. Zhu, S.-T. Xue, Y.-C. Lou, Z.-F. Liu, C. Chen, F. Zhu, *et al.*, Manipulating spatial structure of high-order quantum coherence with entangled photons, *ArXiv:2306.00772* (2023).
- [44] P. Georgi, M. Massaro, K.-H. Luo, B. Sain, N. Montaut, H. Herrmann, T. Weiss, G. Li, C. Silberhorn, and T. Zentgraf, Metasurface interferometry toward quantum sensors, *Light Sci. Appl.* **8**, 70 (2019).
- [45] H. P. Specht, J. Bochmann, M. Mücke, B. Weber, E. Figueroa, D. L. Moehring, and G. Rempe, Phase shaping of single-photon wave packets, *Nat. Photonics* **3**, 469 (2009).
- [46] M. Gilaberte Basset, F. Setzpfandt, F. Steinlechner, E. Beckert, T. Pertsch, and M. Gräfe, Perspectives for applications of quantum imaging, *Laser. Photon. Rev.* **13**, 1900097 (2019).
- [47] M. A. Taylor, J. Janousek, V. Daria, J. Knittel, B. Hage, H.-A. Bachor, and W. P. Bowen, Biological measurement beyond the quantum limit, *Nat. Photonics* **7**, 229 (2013).
- [48] M. Parniak, S. Borówka, K. Boroszko, W. Wasilewski, K. Banaszek, and R. Demkowicz-Dobrzański, Beating the Rayleigh limit using two-photon interference, *Phys. Rev. Lett.* **121**, 250503 (2018).
- [49] S. P. Walborn, A. N. de Oliveira, S. Pádua, and C. H. Monken, Multimode Hong-Ou-Mandel interference, *Phys. Rev. Lett.* **90**, 143601 (2003).
- [50] L.-P. Deng, G.-F. Dang, and K. Wang, Spatial-mode two-photon interference at a beam splitter, *Phys. Rev. A* **74**, 063819 (2006).
- [51] F. Töppel, A. Aiello, and G. Leuchs, All photons are equal but some photons are more equal than others, *New J. Phys.* **14**, 093051 (2012).
- [52] D. Cui, X. Yi, and L.-P. Yang, Quantum imaging exploiting twisted photon pairs, *Adv. Quantum Technol.* **6**, 2370053 (2023).
- [53] L.-P. Yang and Z. Jacob, Non-classical photonic spin texture of quantum structured light, *Commun. Phys.* **4**, 221 (2021).
- [54] C. K. Hong and L. Mandel, Theory of parametric frequency down conversion of light, *Phys. Rev. A* **31**, 2409 (1985).
- [55] C. H. Monken, P. H. S. Ribeiro, and S. Pádua, Transfer of angular spectrum and image formation in spontaneous parametric down-conversion, *Phys. Rev. A* **57**, 3123 (1998).
- [56] A. N. Black, E. Giese, B. Braverman, N. Zollo, S. M. Barnett, and R. W. Boyd, Quantum nonlocal aberration cancellation, *Phys. Rev. Lett.* **123**, 143603 (2019).
- [57] T. B. Pittman, Y. H. Shih, D. V. Strekalov, and A. V. Sergienko, Optical imaging by means of two-photon quantum entanglement, *Phys. Rev. A* **52**, R3429 (1995).

- [58] L. Novotny and B. Hecht, *Principles of Nano-Optics* (Cambridge University Press, Cambridge, England, 2012), Chap. 3.
- [59] J. Mertz, *Introduction to Optical Microscopy* (Cambridge University Press, Cambridge, United Kingdom; New York, NY, 2019), Chap. 3.
- [60] Y. Zhang, F. S. Roux, T. Konrad, M. Agnew, J. Leach, and A. Forbes, Engineering two-photon high-dimensional states through quantum interference, *Sci. Adv.* **2**, e1501165 (2016).
- [61] V. D'Ambrosio, G. Carvacho, I. Agresti, L. Marrucci, and F. Sciarrino, Tunable two-photon quantum interference of structured light, *Phys. Rev. Lett.* **122**, 013601 (2019).
- [62] Z.-F. Liu, C. Chen, J.-M. Xu, Z.-M. Cheng, Z.-C. Ren, B.-W. Dong, Y.-C. Lou, Y.-X. Yang, S.-T. Xue, Z.-H. Liu, W.-Z. Zhu, X.-L. Wang, and H.-T. Wang, Hong-Ou-Mandel interference between two hyperentangled photons enables observation of symmetric and antisymmetric particle exchange phases, *Phys. Rev. Lett.* **129**, 263602 (2022).
- [63] O. S. Magaña Loaiza, M. Mirhosseini, B. Rodenburg, and R. W. Boyd, Amplification of angular rotations using weak measurements, *Phys. Rev. Lett.* **112**, 200401 (2014).
- [64] L.-P. Yang, Geometric phase for twisted light, *Opt. Express* **31**, 10287 (2023).
- [65] C. Alexeyev and M. Yavorsky, Topological phase evolving from the orbital angular momentum of ‘coiled’ quantum vortices, *J. Opt. A: Pure Appl. Opt.* **8**, 752 (2006).
- [66] C. N. Alexeyev and M. A. Yavorsky, Berry’s phase for optical vortices in coiled optical fibres, *J. Opt. A: Pure Appl. Opt.* **9**, 6 (2006).
- [67] W. W. Chow, J. Gea-Banacloche, L. M. Pedrotti, V. E. Sanders, W. Schleich, and M. O. Scully, The ring laser gyro, *Rev. Mod. Phys.* **57**, 61 (1985).
- [68] R. Heintzmann and C. G. Cremer, in *Optical biopsies and microscopic techniques III*, Vol. 3568 (SPIE, 1999), p. 185.
- [69] M. G. Gustafsson, Surpassing the lateral resolution limit by a factor of two using structured illumination microscopy, *J. Microsc.* **198**, 82 (2000).
- [70] R. Loudon, *The Quantum Theory of Light* (Oxford University Press, Oxford, UK, 2000), Chap. 6.
- [71] A. Ritboon, S. Croke, and S. M. Barnett, Optical angular momentum transfer on total internal reflection, *J. Opt. Soc. Am. B* **36**, 482 (2019).
- [72] A. M. Brańczyk, Hong-Ou-Mandel interference, ArXiv: 1711.00080 (2017).